nature chemistry

ARTICLES

PUBLISHED ONLINE: 20 NOVEMBER 2017 | DOI: 10.1038/NCHEM.2886

Theory-driven design of high-valence metal sites for water oxidation confirmed using *in situ* soft X-ray absorption

Xueli Zheng[1,2†], Bo Zhang[1,3*†], Phil De Luna[4†], Yufeng Liang[5], Riccardo Comin[1], Oleksandr Voznyy[1], Lili Han[2,6,7], F. Pelayo García de Arquer[1], Min Liu[1], Cao Thang Dinh[1], Tom Regier[8], James J. Dynes[8], Sisi He[3], Huolin L. Xin[6], Huisheng Peng[3], David Prendergast[5], Xiwen Du[2] and Edward H. Sargent[1*]

The efficiency with which renewable fuels and feedstocks are synthesized from electrical sources is limited at present by the sluggish oxygen evolution reaction (OER) in pH-neutral media. We took the view that generating transition-metal sites with high valence at low applied bias should improve the activity of neutral OER catalysts. Here, using density functional theory, we find that the formation energy of desired Ni^{4+} sites is systematically modulated by incorporating judicious combinations of Co, Fe and non-metal P. We therefore synthesized NiCoFeP oxyhydroxides and probed their oxidation kinetics with *in situ* soft X-ray absorption spectroscopy (sXAS). *In situ* sXAS studies of neutral-pH OER catalysts indicate ready promotion of Ni^{4+} under low overpotential conditions. The NiCoFeP catalyst outperforms IrO_2 and retains its performance following 100 h of operation. We showcase NiCoFeP in a membrane-free CO_2 electroreduction system that achieves a 1.99 V cell voltage at 10 mA cm^{-2}, reducing CO_2 into CO and oxidizing H_2O to O_2 with a 64% electricity-to-chemical-fuel efficiency.

Electrochemical reduction of CO_2 to value-added fuels seeks to reduce the present-day dependence on legacy fossil fuels and thereby mitigate net CO_2 emissions[1–4]. In electrochemical CO_2 reduction, the use of neutral-pH aqueous electrolyte is desired because it provides the highest CO_2 solubility while suppressing the undesired competing hydrogen evolution reaction.

Unfortunately, in pH-neutral electrolytes, the overpotential of the anodic oxygen evolution reaction (OER) is, in the best catalysts reported so far, very high (>460 mV at 10 mA cm^{-2})[3,5–7]. This limits the electrical-to-chemical power conversion efficiency of the overall reaction. To improve the energy efficiency of CO_2 conversion, efforts have been made to provide CO_2 reduction in neutral media while operating OER in alkaline electrolyte. However, the effective overpotential remains high (~430 mV) due to the additional energy needed to overcome the effect of pH gradients[3,8,9], that is, the need also to overcome the membrane potential. Breakthroughs in low-overpotential, stable and earth-abundant OER catalysts that operate optimally at neutral pH are therefore urgently needed to complement rapid advancements in CO_2 reduction electrocatalysts.

High-valence transition-metal (TM) ions incorporated into metal oxides are known to achieve a high reactivity towards water oxidation[5,10–15]. However, as highlighted by their Pourbaix diagrams, TM ions prefer to take on low-valence oxidation states at neutral pH[5,11,16–18]. We thus adopted a new strategy, one in which we would seek to minimize the energy (formation energy) required for active metal sites to reach the desired high oxidation state at neutral pH[5,12]. We hypothesized that a low active-site formation energy would correlate well with a low overpotential to achieve a high-turnover-frequency activated state.

We focused on the well-known Ni^{2+}→Ni^{4+} earth-abundant catalyst[5,12,18]. We sought to challenge our posited correlation experimentally, pursuing *in situ* monitoring of the oxidation state of the OER catalyst.

Multi-metal oxides based on Co, Fe and Ni often outperform unary metal oxides due to modulation of their electronic properties and the resultant fine-tuning of the adsorption energies of the reaction intermediates[10,19–25]. Concomitantly, cobalt-phosphate compounds exhibit high activity at neutral pH[6,11,26]. We reasoned that phosphate could help promote the TM to high valence states and that the catalytic activity of promising multi-metal oxides (that is, 3*d* metals) could be further enhanced if their 3*d* electronic structures were systematically and rationally modulated by incorporating multi-metal and non-metal modulators[19,25,26].

We therefore explored combinations of elements incorporated into Ni oxides in an atomically intimate manner[19], seeking the ready formation of Ni^{4+} with the goal of improving the catalytic activity of the material. We synthesized NiCoFeP oxyhydroxides and probed their oxidation kinetics using *in situ* soft X-ray absorption spectroscopy (sXAS). The new NiCoFeP catalysts exhibit exceptional OER performance, with a 330 mV overpotential at 10 mA cm^{-2} in CO_2-saturated 0.5 M $KHCO_3$ electrolyte. The new catalyst outperforms the leading precious metal oxide IrO_2 and retains its performance after 100 h of operation. We then combined the

[1]Department of Electrical and Computer Engineering, University of Toronto, 35 St George Street, Toronto, Ontario M5S 1A4, Canada. [2]Institute of New-Energy Materials, School of Materials Science and Engineering, Tianjin University, Tianjin 300072, China. [3]State Key Laboratory of Molecular Engineering of Polymers, Department of Macromolecular Science and Laboratory of Advanced Materials, Fudan University, Shanghai 200438, China. [4]Department of Materials Science and Engineering, University of Toronto, 184 College Street, Toronto, Ontario M5S 3E4, Canada. [5]The Molecular Foundry, Lawrence Berkeley National Laboratory, Berkeley, California 94720, USA. [6]Center for Functional Nanomaterials, Brookhaven National Laboratory, Upton, New York 11973, USA. [7]Center for Electron Microscopy, TUT-FEI Joint Laboratory, Institute for New Energy Materials & Low-Carbon Technologies, School of Materials Science and Engineering, Tianjin University of Technology, Tianjin, 300384, China. [8]Canadian Light Source, Inc. (CLSI), 44 Innovation Boulevard, Saskatoon, Saskatchewan S7N 2V3, Canada. †These authors contributed equally to this work. *e-mail: ted.sargent@utoronto.ca; bozhang@fudan.edu.cn

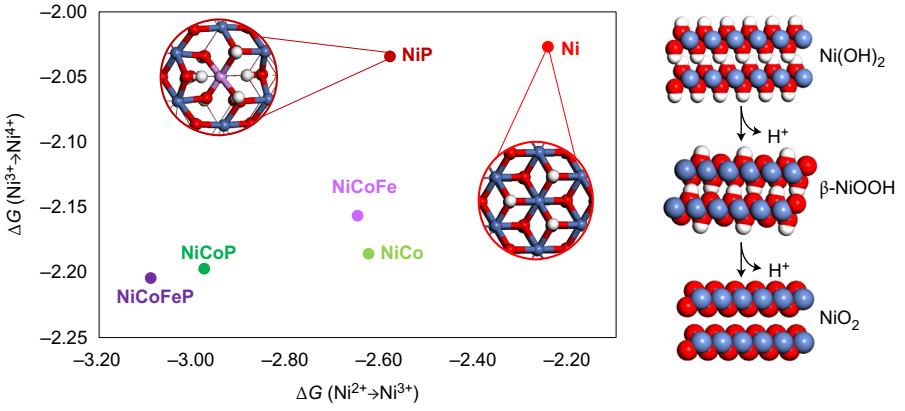

Figure 1 | Change in Gibbs free energies for Ni^{2+}→Ni^{3+}→Ni^{4+}. DFT calculated free energies for the oxidation of $Ni(OH)_2$ to NiO_2 (right-hand column) with various Ni-site substitutions (if any): Ni (red), NiCo (green), NiCoFe (purple). Phosphorus and metal doping promotes the formation of NiO_2 (Ni^{4+}) by lowering the ΔG required for this transition. Doping with phosphorus lowers the change in formation energy for the $Ni(OH)_2$→NiOOH transition (left shift). DFT reveals that the phosphorus dopant prefers to be fourfold coordinated and introduces steric strain in the $Ni(OH)_2$ structure, as shown by the structure magnification of P (purple) and Ni (blue) centres in a P-doped $Ni(OH)_2$ bulk crystal. Similarly, doping with Fe and Co lowers the change in formation energy for the NiOOH→NiO_2 transition (down shift).

optimal multi-metal oxide with a gold nanoneedle CO_2 reduction catalyst to assemble an electrolyser system that converts CO_2 and H_2O into CO and O_2. We found that the new system operated at a low cell voltage of 1.99 V and recorded an electricity-to-chemical-fuel efficiency of 64%.

Results and discussion

Theoretical studies. We began by carrying out computational studies aimed at understanding the effect of intimate metal and phosphorous doping on the stability of nickel structures with different valences. Density functional theory (DFT) calculations with on-site Hubbard-like corrections (DFT + U) were performed on model $Ni(OH)_2$, β-NiOOH and NiO_2 structures (doped with Co, Fe and P) to model Ni^{2+}, Ni^{3+} and Ni^{4+} oxidation states, respectively (see Supplementary Table 1 for the optimized lattice constants). Experimentally, the NiO_2 phase is unstable and does not exist in the Ni Pourbaix diagram; simulations reproduce this observation, showing that NiO_2 formation is unfavourable by 0.31 eV per formula unit (f.u.).

However, once NiO_2 is doped with phosphorus or other metals, the formation energies become negative, indicating a more stable phase (Supplementary Table 2). The simulations thus suggest that doping using Co, Fe and P can lower the Gibbs formation energy of compounds containing Ni^{4+} that are otherwise unstable.

The oxidation of Ni^{2+} to Ni^{4+} comprises the following proton-coupled electron transfer reactions[27]:

$$Ni(OH)_2 \rightarrow NiOOH + H^+ + e^- \quad (1)$$

$$NiOOH \rightarrow NiO_2 + H^+ + e^- \quad (2)$$

We found that substitutional doping of nickel to phosphorus consistently lowered the Ni^{2+}→Ni^{3+} reaction free energies, while substitution of Ni with Co and Fe lowered the Ni^{3+}→Ni^{4+} reaction free energies (Fig. 1). Phosphorus, which prefers a fourfold coordination, affects nearby hydrogen geometries and induces steric strain into the lattice, resulting in destabilization of the $Ni(OH)_2$ phase. Moreover, Co and Fe in ternary blends modulate the electronic structure of the nickel oxides, stabilizing the Ni^{4+} phase.

To investigate the modulation of electronic structure with respect to TM doping, we carried out a density of states (DOS) analysis. It was found that the valence band maximum (VBM) was only 0.17 eV below the Fermi level for NiO_2, but for $Ni(OH)_2$ it was 0.20 eV below the Fermi level. This suggests that the Ni^{4+} shifts the Fermi level down compared to Ni^{2+} to expose hole states for catalysis[28]. From a DOS comparison of NiO_2 and $Ni_{1-x-y}Co_xFe_yO_2$, we found that the NiCoFe oxide introduces more *d* states within the gap than pure NiO_2 (Supplementary Fig. 1). A projected DOS (pDOS) analysis (Supplementary Fig. 2) revealed that electronic states near the Fermi level are predominantly from Ni and Fe 3*d* orbitals, suggesting that both Fe^{4+} and Ni^{4+} can act as catalytic active sites, as they each contribute states near the valence band-edge[29].

Oxidation-state changes monitored by *in situ* sXAS. To challenge, experimentally, the concept that low formation energy could correlate with an early voltage onset of efficient OER, we sought a means to track the electronic states of metal sites *in situ*. Hard X-ray absorption spectroscopy (hXAS) has previously been used *in situ* to probe high-energy transitions between 1*s* and 4*p* electronic orbitals and is more relevant to local coordination environments. The electronically relevant 3*d* final state is weakly evident in hXAS as a low-intensity pre-edge feature resulting from quadrupole transitions[30]. For this reason, the hXAS pre-edges do not enable an informative determination of the narrowband, TM 3*d* electronic structure. Real-time tracking of the X-ray absorption near-edge region of the Ni K-edge was used to obtain initial information about their valence states and electronic configurations[31].

We turned instead to sXAS at the TM $L_{2,3}$-edges, which accurately and efficiently quantifies the TM oxidation states because these dipole-allowed 2*p*→3*d* optical transitions probe directly the 3*d* states that are crucial to chemical activities. It provides detailed information on the local electronic structure and is sensitive to chemical bonding and oxidation states[32–37]. sXAS measurements were performed by recording the partial fluorescence yield (PFY) intensity. The spectra are not strictly proportional to the X-ray attenuation coefficient due to state-dependent decay probabilities[32]. These electron delocalization effects are known to enhance the fluorescence intensities of the higher-energy transitions in an L-edge PFY spectrum. We considered these effects in our interpretation of the *in situ* measurements. We concluded that the magnitude of the bias-dependent changes we observed was much greater than the small effects arising due to state-dependent decay[33].

One challenge in using sXAS to study *in situ* operating OER catalysts arises from its limited probe depth. sXAS does not reveal the (remote, far-side) active surface behaviour of an operating catalyst when excited and probed through a window and substrate (Fig. 2). We therefore synthesized highly nanoporous NiCoFeP

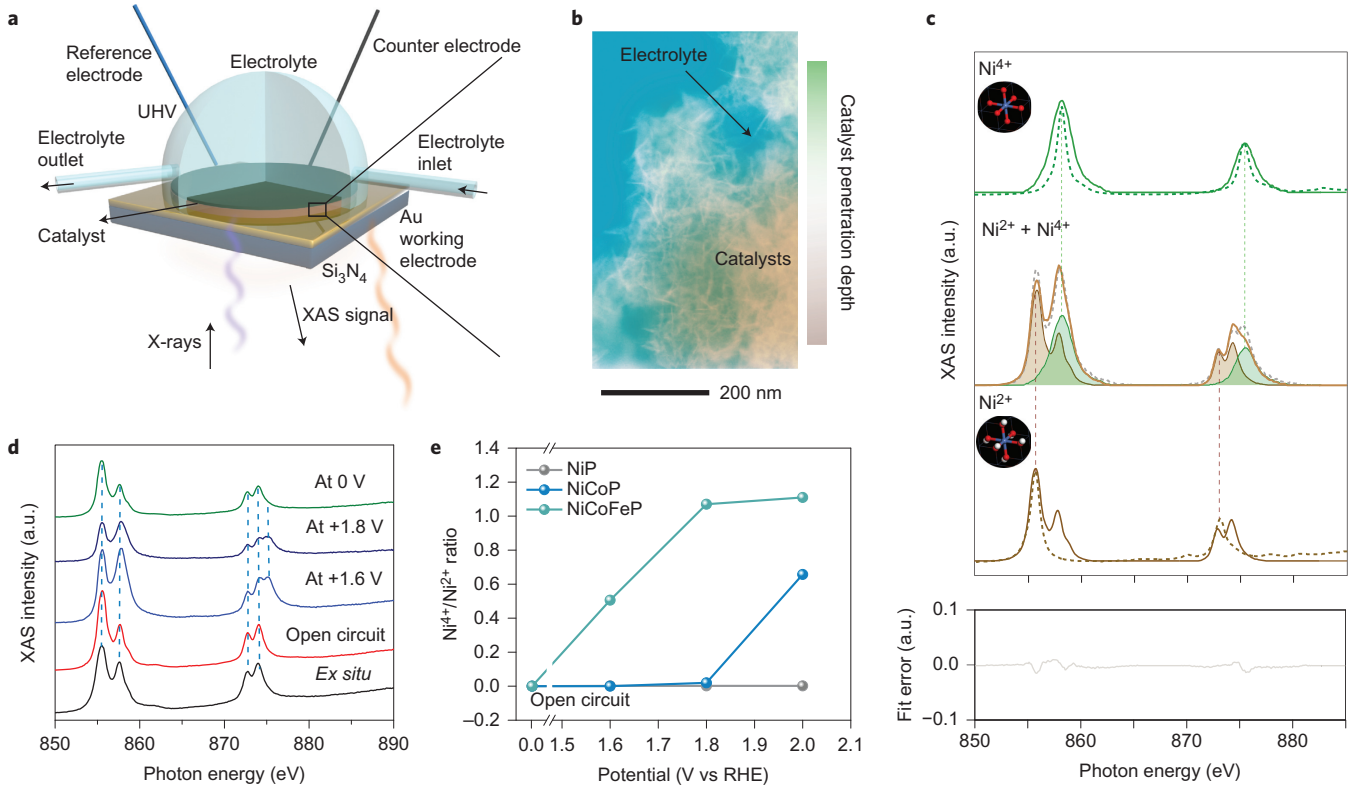

Figure 2 | An *in situ* electrochemical flow cell, enabling *in situ* sXAS. a,**b**, Schematic illustration of the *in situ* liquid cell experimental set-up (**a**) and a STEM image of the NiCoFeP catalyst (**b**). A Si_3N_4 membrane (~100 nm) separates the liquid from the high-vacuum region where soft X-rays propagate. Detection of X-ray absorption was performed by collecting X-ray fluorescence on the vacuum side. **c**, *In situ* experimental (solid lines) and theoretical (dashed lines) sXAS at the Ni L-edge of Ni^{2+} (brown) and Ni^{4+}(green), respectively. The theoretical sXAS is aligned according to the L_3-edge of Ni^{2+}. The top spectra, obtained for NiCoFeP at +1.8 V versus RHE during the reaction, was fitted by experimental sXAS data for NiO (Ni^{2+}), $LiNiO_2$ (Ni^{3+}) and potassium nickel(IV) paraperiodat $K_2Ni(H_2IO_6)_2$ (Ni^{4+}) references after subtracting Ni^{2+} signals. **d**, Ni L-edge of NiCoFeP and relevant controls. **e**, Ni^{4+}/Ni^{2+} ratio versus potential for NiCoFeP and controls.

samples in the expectation that the electrolyte used in OER might substantially penetrate into them. We employed an *in situ* electrochemical flow cell with an ultrathin Si_3N_4 membrane window (100 nm thick) to separate the liquid medium inside the cell from the high-vacuum environment needed for soft X-ray measurements (Fig. 2a). The working electrode for loading catalysts consisted of an ~20 nm Au film evaporated on the internal side of a Si_3N_4 membrane, in contact with a flowing CO_2-saturated 0.5 M $KHCO_3$ solution as the electrolyte. Scanning transmission electron microscopy (STEM) images of NiCoFeP reveal a structure composed of nanosheets and nanopores (Fig. 2b). Energy-dispersive X-ray spectroscopy (EDS) mapping (Supplementary Fig. 7) and electron energy loss spectroscopy (EELS) elemental maps with sub-nanometre resolution (Supplementary Fig. 9) show a uniform, uncorrelated spatial distribution of Ni, Co, Fe and P with a 9:1:1:0.1 atomic ratio, as determined by inductively coupled plasma atomic emission spectrometry (ICP-AES) analysis (Supplementary Fig. 10).

As a result of 2*p* core hole spin–orbit splitting, both the experimental and theoretical Ni L-edge XAS spectra (Fig. 2c) are divided into two regions of interest: the L_3-edge near 856 eV and the L_2-edge near 874 eV. High-resolution sXAS spectra can also resolve the fine multiplet structure arising from Ni 2*p*–3*d* interactions and crystal field effects from the modulated local coordination environment[34,36]. We first measured the Ni L-edges using PFY on samples prepared *ex situ*, and observed no difference compared to open-circuit potential conditions (Fig. 2d). We then acquired PFY at the Ni L-edge, with a probe depth of ~300 nm, collecting real-time spectra while applying a constant anodic bias of +1.6 V, +1.8 V and +2.0 V versus RHE (reversible hydrogen electrode), respectively (Supplementary Fig. 12).

To understand the changes in the Ni L-edge, we carried out first-principles calculations, solving the Bethe–Salpeter equation (BSE) for correlated electrons and holes with the goal of predicting theoretical sXAS spectra with the aid of the OCEAN simulation package[38,39]. The BSE is capable of reproducing the branching ratio of the L_3/L_2-edges correctly[38], together with the edge shift, in different chemical environments or oxidation states[40]. We used ground-state DFT + U Kohn–Sham orbitals as input for the BSE calculation, with $U = 6.45$ eV, identical to our formation energy calculations. Our BSE calculations, working within a basis of single electron–hole pair excitations, cannot describe atomic multiplet splitting. In particular, for the Ni^{2+} system, the L_3-edge is split into a main peak and a secondary feature at higher energies. To reproduce multiplet effects, we also performed an atomic configuration calculation with the CTM4XAS code (downloadable from http://www.anorg.chem.uu.nl/CTM4XAS/)[41,42]. The magnitude of the crystal field splitting was chosen to be 2.0 eV, which was estimated from the DFT + U calculation for the layered $Ni(OH)_2$ structure. With the multiplet effects included, the simulated spectrum of Ni^{2+} is in excellent agreement with experiments.

These *in situ* sXAS studies provide the first direct view of Ni^{4+} as it forms during the operation of oxyhydroxide catalysts during water oxidation. We performed NiO (Ni^{2+}), $LiNiO_2$ (Ni^{3+}) and potassium nickel(IV) paraperiodat $K_2Ni(H_2IO_6)_2$ (Ni^{4+}) references at Beijing Light Source 4W1B beamline (Supplementary Fig. 4). We chose $LiNiO_2$ as our Ni^{3+} reference because it has a layered double hydroxide structure. We subtracted Ni^{2+} from the potassium nickel(IV)

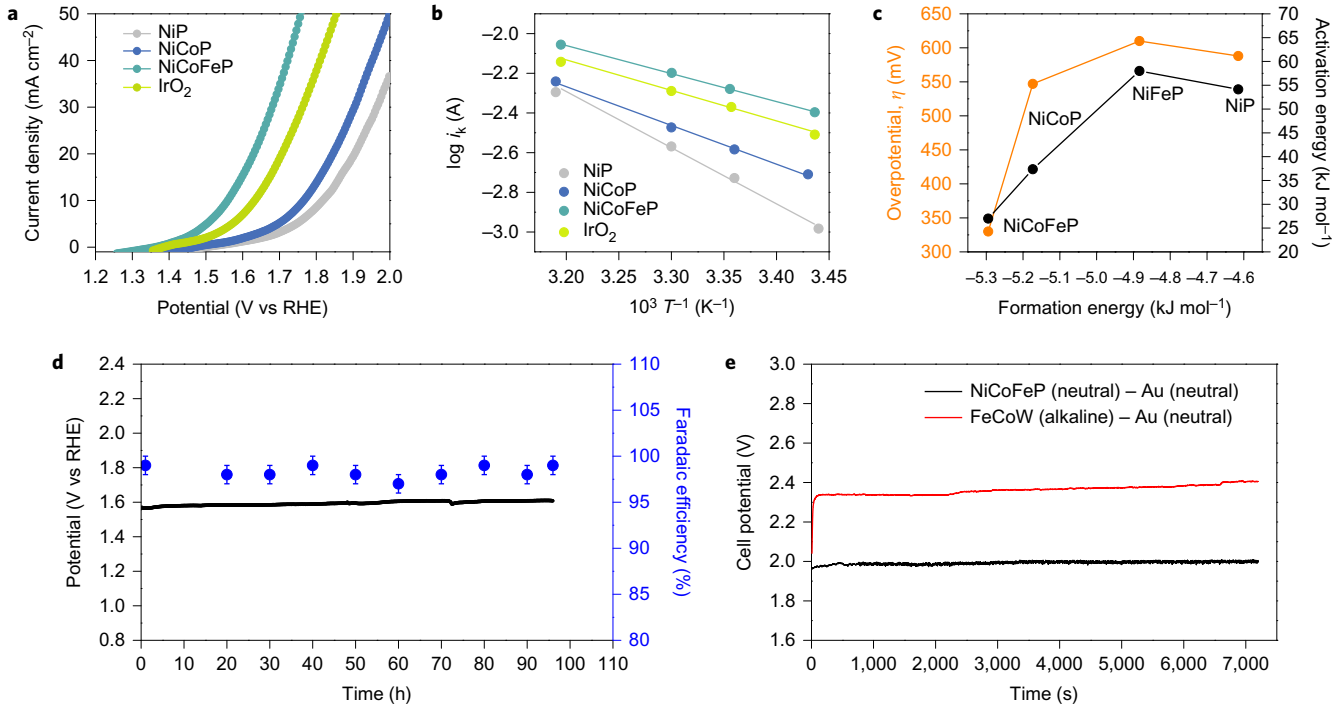

Figure 3 | Performance of NiCoFeP oxyhydroxides catalysts and controls in a three-electrode configuration in CO_2-saturated 0.5 M $KHCO_3$ aqueous electrolyte. a, The OER polarization curve of catalysts loaded on Au foam at a scan rate of 1 mV s^{-1}. **b**, Arrhenius plot of inverse temperature versus log of exchange current for NiCoFeP oxyhydroxides and controls on Au (111). **c**, Relation between overpotential at 10 mA cm^{-2} (left axis), activation energy (right axis) and the theoretical formation energy of Ni^{2+} to Ni^{4+} in NiCoFeP and controls. Solid lines are shown for guidance only. **d**, Chronopotentiometric curves obtained with the NiCoFeP on gold-plated Ni foam electrode with constant current densities of 10 mA cm^{-2} (left axis) and the corresponding Faradaic efficiency from gas chromatography measurement of evolved O_2 (right axis). Each point was measured five times independently to obtain the average value and the absolute error. **e**, Cell potential as function of time for CO_2 electrolysis at a controlled current density of 10 mA cm^{-2} (see Supplementary Fig. 22a for a scheme of NiCoFeP–Au needles electrolysis (black line) and Supplementary Fig. 22b for a scheme of FeCoW–Au needles with a bipolar membrane (red line)).

paraperiodat $K_2Ni(H_2IO_6)_2$ (Ni^{4+}) reference and obtained a single-peak shape similar to our simulated spectra. The intensity ratio of the double-peak features in the Ni-L_3 region, at 855.6 and 857.5 eV, provides one qualitative proxy for the relative proportion of the two Ni oxidation state populations of interest; that is, it captures the progression from Ni^{2+} to Ni^{3+} and Ni^{4+} upon application of a potential in the NiCoFeP sample (Supplementary Fig. 12). The emergence of an additional, broader peak at the Ni L_2-edge around 875.1 eV confirms the generation of Ni^{4+} species (Fig. 2d). The relative L_3-edge chemical shift between Ni^{2+} and Ni^{4+} is also consistent with our BSE calculation, which predicts a blueshift of 2.6 eV from Ni^{2+} to Ni^{4+} (dashed curves in Fig. 2c). Both the Ni L_3- and L_2-edge sXAS results revert back to their original state when a cathodic bias (0 V versus RHE) is applied in the NiCoFeP sample. This suggests a return to the low Ni oxidation state and paints a picture of the reversible redox of Ni^{4+}/Ni^{2+} (Fig. 2d).

We also acquired Ni *in situ* sXAS while varying the potentials for NiCoP (Supplementary Fig. 13) and NiP (Supplementary Fig. 14). The NiCoP sample exhibited a significantly lower Ni^{4+}/Ni^{2+} ratio than the NiCoFeP sample at various potentials (Fig. 2e and Supplementary Fig. 13). In NiP, we detected no ostensible changes in the oxidation state, even in the presence of a 2.0 V potential (Supplementary Fig. 14), consistent with the DFT prediction of the high formation energy of Ni^{4+} in NiP.

Overall, the *in situ* studies agree with a physical picture in which Ni is the ionic species most susceptible to becoming oxidized to high valence in NiCoFeP, and where the incorporation of Co, Fe and P beneficially modulates the electronic structure of Ni metal oxides. It results in a reduced formation energy for Ni^{4+}, a configuration favourable for water oxidation, consistent with the DFT studies in this work.

We also used *in situ* XAS at the Fe and Co L-edges of NiCoFeP and relevant controls. *In situ* spectra of the Fe L-edge indicate that Fe^{3+} remains the dominant valence state before and during electrochemical operation (Supplementary Fig. 15), while the valence state of Co evolves from Co^{2+} under open-circuit conditions to Co^{3+} upon application of a potential, including only a modest admixture with Co^{2+} in all samples (Supplementary Fig. 16).

Water oxidation electrocatalysis. We next proceeded to compare the catalytic performance of NiCoFeP with that of the reference samples NiP, NiCoP and IrO_2 for the OER. To increase the conductivity of the electrode, we loaded our catalysts on a gold-plated nickel foam. Representative OER currents were measured in CO_2-saturated 0.5 M $KHCO_3$ aqueous electrolyte at a scan rate of 1 mV s^{-1} (Fig. 3a) (currents are uncorrected and thus are already penalized by the effects of resistive losses incurred within the electrolyte).

The NiCoFeP-on-gold-plated Ni foam requires an overpotential of only 330 mV at 10 mA cm^{-2} (Table 1, all current densities based on projected geometric area), which is 70 mV lower than that of the best commercial precious-metal-oxide IrO_2 catalyst tested under identical conditions. To the best of our knowledge, this is the first report of an earth-abundant catalyst that consistently outperforms precious-metal-oxide catalysts in a pH-neutral medium[3,5–7] (Table 1). To evaluate the effect of surface area using an additional independent method, we analysed the surface area via the Brunauer, Emmett and Teller (BET) technique. This allowed us to report the normalized kinetic current density (referred to as 'specific activity') as a function of potential versus RHE to assess the intrinsic activities of the catalysts. Using this metric, the intrinsic activity of NiCoFeP oxyhydroxide was confirmed to be notably higher than that of the

Table 1 | Comparison of catalytic parameters of NiCoFeP and controls.

Samples	pH	On gold foam Overpotential η (mV) at 10 mA cm^{-2}	On glassy carbon Overpotential η (mV) at 1 mA cm^{-2}	On Au(111) ΔH (kJ mol^{-1}) at η = 700 mV	Ref.
NiP	7.2	588	390	54.14	This work
NiCoP	7.2	547	330	37.36	This work
NiCoFeP	7.2	330	276	27.00	This work
Commercial IrO_2	7.2	400	-	29.41	This work
IrO_2	7.2	460*	290*	-	3
MnO_2	7.5	-	417†	-	43
Ni-based	6.8	-	467	-	7
Co-Pi	7.0	-	550†	-	6

*Current density obtained on Ti plate. †Current density obtained on a conductive glassy substrate.

controls (Supplementary Fig. 17). From BET, the high catalytic activity of NiCoFeP oxyhydroxide includes an appreciable intrinsic (not surface-area-related) contribution.

To assess the kinetic barriers involved in OER, we studied the effect of temperature on the performance of the catalysts (Fig. 3b and Supplementary Fig. 19). OER proceeds more rapidly at elevated temperatures, with an exponential temperature dependence of the chemical rate constant[43]. The electrochemical activation energies extracted from the slopes of the Arrhenius plots are lower for the new catalyst than for IrO_2 (Table 1 and Supplementary Fig. 16). The most active NiCoFeP catalysts in this study exhibit an apparent barrier value of 27 kJ mol^{-1}, indicating high catalytic activity.

Our studies suggest that developing a TM oxyhydroxide with lower Ni^{4+} formation energy provides an effective strategy and new avenue to enhance OER catalytic activity (Fig. 3c). To characterize the performance stability, we operated the OER catalyst on gold-plated Ni foam under a constant current density of 10 mA cm^{-2} continuously for 100 h. We observed no appreciable increase in potential (Fig. 3d) over this time period. To verify that the catalyst remained physically intact, we checked using ICP-AES for any observable leaching of the constituents into the electrolyte. We were able to detect no measurable elemental loss using this sensitive method. Consistently high activity throughout the entire duration of stability testing was further confirmed by measuring the rate of O_2 evolution from the NiCoFeP-on-gold-plated Ni foam catalyst. We obtained quantitative (that is, unity Faradaic efficiency) gas evolution of oxygen to within our available ±5% experimental error. Our approach to minimize the formation energy required for active metal sites may also open up further avenues to other related oxidation reactions.

We next assembled an electrolyser that converts CO_2 and H_2O into CO and O_2 based on NiCoFeP oxyhydroxides as OER catalysts and recently reported Au nanoneedles as CO_2 reduction catalysts[44]. We achieved a 1.99 V cell voltage at 10 mA cm^{-2}, with an electricity-to-chemical-fuel efficiency of 64% (Fig. 3e). This was accomplished in a membrane-free system that avoids membrane resistance. In contrast, when we use a H-cell electrolyser with bipolar membranes, which enabled the use of the state-of-the-art OER catalyst FeCoW in a favourable alkaline electrolyte, the total cell potential reached 2.37 V and achieved a 54% electricity-to-chemical-fuel efficiency (Supplementary Table 3). The new neutral OER catalysts reported herein provide efficient membrane-free electrolysis and thus represent an overall enabling component in CO_2 reduction.

Methods

Energetics calculations. The bulk energetics of metal- and phosphorous-doped Ni-oxides were calculated using DFT with the Hubbard–U framework (DFT + U) to account for the strongly localized *d* electrons for Ni, Fe and Co. The Perdew–Burke–Ernzerhof (PBE) exchange-correlation functional and Blöchl's all-electron, frozen-core, projector augmented (PAW) method with a plane-wave basis set cutoff value of 750 eV were used with the Vienna Ab-initio Simulation Package (VASP). The Gibbs free energy of formation, $\Delta G°_f$, was calculated using the framework of Persson *et al.*[17] where the reference energies are taken from the most stable phase of each element. For full details see Supplementary Section 'Structures of models used'.

Synthesis of gelled NiCoFeP oxyhydroxides and controls. All gelled oxyhydroxides were synthesized using a modified aqueous sol–gel technique[16].

***In situ* X-ray absorption.** X-ray absorption measurements at the Ni, Co and Fe L-edges were performed at the Spherical Grating Monochromator (SGM) beamline 11ID-1 at the Canadian Light Source. The window of the sample cells was mounted at an angle of roughly 45° with respect to both the incident beam and the detectors. The bodies of the sample cells were fabricated on an Object Connex500 printer by three-dimensional printing with DurusWhite material. The catalysts were coated on the windows via dropcasting with a thickness of 400 nm. The gold-covered window was contacted by gold wires. Silver and platinum wires were used as reference and counter electrodes. All measurements were made at room temperature in fluorescence mode using Amptek silicon drift detectors (SDDs) with 1,024 emission channels (energy resolution ~120 eV). Four SDDs were used simultaneously. The scanning energy ranges of Ni, Co and Fe L-edges were set between 840 and 900 eV, 760 and 820 eV, and 690 and 750 eV, respectively. The PFY was extracted from all SDDs by summation of the corresponding metal L emission lines. For full details see Supplementary Figs 12–16.

L-edge simulation of XAS with the OCEAN code. The formalism of the BSE is provided in ref. 38. The input DFT + U calculations were performed using norm-conserving pseudopotentials. A very large energy cutoff of 160 Ryd was used for the plane-wave basis set of the Kohn–Sham wavefunctions. The key part of the electron–core–hole interactions is the screened Coulomb interaction, which is obtained within the random phase approximation. A large number of empty bands up to 50 eV above the Fermi level were included in the calculations. A 6 × 6 × 6 k-grid over the Brillouin zone was used to produce the sXAS spectra, which were convoluted with Lorentzians of 0.5 eV.

Electrochemical measurements. Electrochemical measurements were performed using a three-electrode system connected to an electrochemical workstation (Autolab PGSTAT302N). Cyclic voltammetry (CV) measurements at 50 mV s^{-1} were performed for three cycles before recording linear scan voltammetry (LSV) at 1 mV s^{-1} for each sample. The LSV performance of NiCoFeP, NiCoP, NiP and the corresponding controls with no phosphorus were also normalized by the BET surface area. The apparent electrochemical activation energy (E_a) for water oxidation was determined using the Arrhenius relationship. Calibrations of the Ag/AgCl reference electrode and Ag wire reference electrode were conducted in the standard three-electrode system (the same system as that for performance measurements) as reference electrodes, using Pt foil as the working and counter electrodes. For full details see Supplementary Figs 17–20.

Data availability. The data supporting the findings of this study are available within this Article and its Supplementary Information files, or from the corresponding author upon reasonable request. The Supplementary Information contains descriptions of methods, and Supplementary Figs 1–29 present results and discussions, assessment of electronic structures, and DFT calculations.

Received 29 August 2016; accepted 29 September 2017; published online 20 November 2017

References

1. Lin, S. *et al.* Covalent organic frameworks comprising cobalt porphyrins for catalytic CO_2 reduction in water. *Science* **349,** 1208–1213 (2015).
2. Goeppert, A., Czaun, M., Jones, J. P., Surya Prakash, G. K. & Olah, G. A. Recycling of carbon dioxide to methanol and derived products—closing the loop. *Chem. Soc. Rev.* **43,** 7995–8048 (2014).
3. Schreier, M. *et al.* Efficient photosynthesis of carbon monoxide from CO_2 using perovskite photovoltaics. *Nat. Commun.* **6,** 7326 (2015).

4. Costentin, C., Drouet, S., Robert, M. & Saveant, J. M. A local proton source enhances CO_2 electroreduction to CO by a molecular Fe catalyst. *Science* **338,** 90–94 (2012).
5. Bediako, D. K. *et al.* Structure–activity correlations in a nickel-borate oxygen evolution catalyst. *J. Am. Chem. Soc.* **134,** 6801–6809 (2012).
6. Kanan, M. W. & Nocera, D. G. *In situ* formation of an oxygen-evolving catalyst in neutral water containing phosphate and Co^{2+}. *Science* **321,** 1072–1075 (2008).
7. Joya, K. S., Joya, Y. F. & de Groot, H. J. M. Ni-based electrocatalyst for water oxidation developed *in-situ* in a HCO_3^-/CO_2 system at near-neutral pH. *Adv. Energy Mater.* **4,** 1301929 (2014).
8. Vargas-Barbosa, N. M., Geise, G. M., Hickner, M. A. & Mallouk, T. E. Assessing the utility of bipolar membranes for use in photoelectrochemical water-splitting cells. *ChemSusChem* **7,** 3017–3020 (2014).
9. Hernández-Pagán, E. A. *et al.* Resistance and polarization losses in aqueous buffer–membrane electrolytes for water-splitting photoelectrochemical cells. *Energy Environ. Sci.* **5,** 7582–7589 (2012).
10. Chen, J. Y. *et al.* Operando analysis of NiFe and Fe oxyhydroxide electrocatalysts for water oxidation: detection of Fe^{4+} by Mossbauer spectroscopy. *J. Am. Chem. Soc.* **137,** 15090–15093 (2015).
11. Bergmann, A. *et al.* Reversible amorphization and the catalytically active state of crystalline Co_3O_4 during oxygen evolution. *Nat. Commun.* **6,** 8625 (2015).
12. Bediako, D. K., Surendranath, Y. & Nocera, D. G. Mechanistic studies of the oxygen evolution reaction mediated by a nickel-borate thin film electrocatalyst. *J. Am. Chem. Soc.* **135,** 3662–3674 (2013).
13. Zaffran, J. & Toroker, M. C. Designing efficient doped NiOOH catalysts for water splitting with first principles calculations. *ChemistrySelect* **1,** 911–916 (2016).
14. Zaffran, J. & Toroker, M. C. Benchmarking density functional theory based methods to model NiOOH material properties: Hubbard and van der Waals corrections vs hybrid functionals. *J. Chem. Theory. Comput.* **12,** 3807–3812 (2016).
15. Li, N., Bediako, D. K., Hadt, R. G. *et al.* Influence of iron doping on tetravalent nickel content in catalytic oxygen evolving films. *Proc. Natl Acad. Sci. USA* **114,** 1486–1491 (2017).
16. Bajdich, M., Garcia-Mota, M., Vojvodic, A., Norskov, J. K. & Bell, A. T. Theoretical investigation of the activity of cobalt oxides for the electrochemical oxidation of water. *J. Am. Chem. Soc.* **135,** 13521–13530 (2013).
17. Persson, K. A., Waldwick, B., Lazic, P. & Ceder, G. Prediction of solid-aqueous equilibria: scheme to combine first-principles calculations of solids with experimental aqueous states. *Phy. Rev. B* **85,** 235438 (2012).
18. Smith, R. D. & Berlinguette, C. P. Accounting for the dynamic oxidative behavior of nickel anodes. *J. Am. Chem. Soc.* **138,** 1561–1567 (2016).
19. Zhang, B. *et al.* Homogeneously dispersed, multimetal oxygen-evolving catalysts. *Science* **352,** 6283–6288 (2016).
20. Gong, M. *et al.* An advanced Ni-Fe layered double hydroxide electrocatalyst for water oxidation. *J. Am. Chem. Soc.* **135,** 8452–8455 (2013).
21. Diaz-Morales, O., Ledezma-Yanez, I., Koper, M. T. M. & Calle-Vallejo, F. Guidelines for the rational design of Ni-based double hydroxide electrocatalysts for the oxygen evolution reaction. *ACS Catal.* **5,** 5380–5387 (2015).
22. Wang, H. *et al.* Bifunctional non-noble metal oxide nanoparticle electrocatalysts through lithium-induced conversion for overall water splitting. *Nat. Commun.* **6,** 7261 (2015).
23. Suntivich, J., May, K. J., Gasteiger, H. A., Goodenough, J. B. & Shao-Horn, Y. A perovskite oxide optimized for oxygen evolution catalysis from molecular orbital principles. *Science* **334,** 1383–1385 (2011).
24. Favaro, M., Drisdell, W. S., Marcus, M. A. *et al.* An operando investigation of (Ni–Fe–Co–Ce) O_x system as highly efficient electrocatalyst for oxygen evolution reaction. *ACS Catal.* **7,** 1248–1258 (2017).
25. Diaz-Morales, O., Ferrus-Suspedra, D. & Koper, M. T. M. The importance of nickel oxyhydroxide deprotonation on its activity towards electrochemical water oxidation. *Chem. Sci.* **7,** 2639–2645 (2016).
26. Kanan, M. W., Surendranath, Y. & Nocera, D. G. Cobalt-phosphate oxygen-evolving compound. *Chem. Soc. Rev.* **38,** 109–114 (2009).
27. Tkalych, A. J., Yu, K. & Carter, E. A. Structural and electronic features of β-$Ni(OH)_2$ and β-NiOOH from first principles. *J. Phys. Chem. C* **119,** 24315–24322 (2015).
28. Carpenter, M. K. & Corrigan, D. A. Photoelectrochemistry of nickel-hydroxide thin-films. *J. Electrochem. Soc.* **136,** 1022–1026 (1989).
29. Friebel, D. *et al.* Identification of highly active Fe sites in (Ni,Fe)OOH for electrocatalytic water splitting. *J. Am. Chem. Soc.* **137,** 1305–1313 (2015).
30. Vinson, J. & Rehr, J. J. *Ab initio* Bethe–Salpeter calculations of the X-ray absorption spectra of transition metals at the L-shell edges. *Phys. Rev. B* **86,** 195135 (2012).
31. Deb, A., Bergmann, U., Cramer, S. P. & Cairns, E. J. Local structure of $LiNi_{0.5}Mn_{0.5}O_2$ cathode material probed by *in situ* X-ray absorption spectroscopy. *J. Appl. Phys.* **99,** 063701 (2006).
32. De Groot, F. M. F. *et al.* 1*s*2*p* resonant inelastic X-ray scattering of iron oxides. *J. Phys. Chem. B* **109,** 20751–20762 (2005).
33. Velasco-Velez, J. J. *et al.* The structure of interfacial water on gold electrodes studied by X-ray absorption spectroscopy. *Science* **346,** 831–834 (2014).
34. Van Veenendaal, M. A. & Sawatzky, G. A. Doping dependence of Ni 2*p* X-ray-absorption spectra of $M_xNi_{1-x}O$ (*M*=Li,Na). *Phys. Rev. B* **50,** 11326–11331 (1994).
35. Liu, X. *et al.* Distinct charge dynamics in battery electrodes revealed by *in situ* and operando soft X-ray spectroscopy. *Nat. Commun.* **4,** 2568 (2013).
36. Van Elp, J., Eskes, H., Kuiper, P. & Sawatzky, G. A. Electronic structure of Li-doped NiO. *Phys. Rev. B* **45,** 1612–1622 (1992).
37. Ralston, C. Y. *et al.* Characterization of heterogeneous nickel sites in CO dehydrogenases from *Clostridium thermoaceticum* and *Rhodospirillum rubrum* by nickel L-edge X-ray spectroscopy. *J. Am. Chem. Soc.* **122,** 10553–10560 (2000).
38. Vinson, J., Rehr, J. J., Kas, J. J. & Shirley, E. L. Bethe–Salpeter equation calculations of core excitation spectra. *Phys. Rev. B* **83,** 115106 (2011).
39. Gilmore, K. *et al.* Efficient implementation of core-excitation Bethe–Salpeter equation calculations. *Comput. Phys. Commun.* **197,** 109–117 (2015).
40. Vinson, J., Kas, J. J., Vila, F. D., Rehr, J. J. & Shirley, E. L. Theoretical optical and X-ray spectra of liquid and solid H_2O. *Phys. Rev. B* **85,** 045101 (2012).
41. Stavistki, E. & de Groot, F. M. F. The CTM4XAS program for EELS and XAS spectral shape analysis of transition metal L edges. *Micron* **41,** 687–694 (2010).
42. Haverkort, M. W., Zwierzycki, M. & Andersen, O. K. Multiplet ligand-field theory using Wannier orbitals. *Phys. Rev. B* **85,** 165113 (2012).
43. Yamaguchi, A. *et al.* Regulating proton-coupled electron transfer for efficient water splitting by manganese oxides at neutral pH. *Nat. Commun.* **5,** 4256–4266 (2014).
44. Liu, M. *et al.* Enhanced electrocatalytic CO_2 reduction via field-induced reagent concentration. *Nature* **537,** 382–386 (2016).

Acknowledgements

This work was supported by the Ontario Research Fund Research Excellence Program, NSERC and the CIFAR Bio-Inspired Solar Energy programme. X.Z. acknowledges a scholarship from the China Scholarship Council (CSC) (20140625004) and the National Basic Research Program of China (2014CB931703). B.Z. acknowledges funding from STCSM (16JC1400702 and 14ZR14110200), NSFC (21503079) and the China Scholarship Council/University of Toronto Joint Funding Program (201406745001). This work has also benefited from SGM beamlines at the Canadian Light Source (CLS) and 4B9B and 4B7A beamlines at Beijing Synchrotron Radiation Facility. The CLS is supported by the Natural Sciences and Engineering Research Council of Canada, the National Research Council Canada, the Canadian Institutes of Health Research, the Province of Saskatchewan, Western Economic Diversification Canada and the University of Saskatchewan. The authors thank J. Guo and L. Zhang from Advanced Light Source for soft X-ray absorption measurements. The TEM study in this work was supported by the Center for Functional Nanomaterials, which is a US DOE Office of Science Facility at Brookhaven National Laboratory, under contract no. DE-SC0012704. First-principles simulations of X-ray absorption spectroscopy and associated interpretation and consultation by Y.L. and D.P. are provided through a user project at The Molecular Foundry (TMF), including use of its computer cluster (vulcan), managed by the High Performance Computing Services Group, at Lawrence Berkeley National Laboratory (LBNL), and associated use of TMF computing resources at the National Energy Research Scientific Computing Center (NERSC), LBNL. TMF and NERSC are US DOE User Facilities, both supported by the Office of Science of the US DOE under contract no. DE-AC02-05CH11231. DFT computations were performed using the IBM BlueGene/Q supercomputer at the SciNet HPC Consortium provided through the Southern Ontario Smart Computing Innovation Platform (SOSCIP).

Author contributions

E.H.S., D.P. and B.Z. supervised the project. X.Z. and B.Z. designed and carried out the experiments. X.Z., B.Z., T.R., J.D. and R.C. performed the soft X-ray measurements. P.D.L., Y.L., D.P. and O.V. carried out simulations. L.H., H.L.X. and X.D. performed TEM measurements. X.Z., B.Z., F.P.C.d.A., M.L., C.T.D., S.H. and H.P. performed electrochemical measurements. All authors discussed the results and assisted during manuscript preparation.

Additional information

Supplementary information is available in the online version of the paper. Reprints and permissions information is available online at www.nature.com/reprints. Publisher's note: Springer Nature remains neutral with regard to jurisdictional claims in published maps and institutional affiliations. Correspondence and requests for materials should be addressed to B.Z. and E.H.S.

Competing financial interests

The authors declare no competing financial interests.